Journal of Sound and Vibration 641 (2026) 119899

Contents lists available at ScienceDirect

Journal of Sound and Vibration

journal homepage: www.elsevier.com/locate/jsvi

Tunable encoding of multiple resonators via layer coupling and its application on vibration localization

Wenqu Li [a], Yuhang Lin [a], Tianqi Li [a], Jingkai Huang [a], Hao Huang [a], Qingbo He [a,*], Zhike Peng [a,b], Li Cheng [c]

[a] *State Key Laboratory of Mechanical System and Vibration, Shanghai Jiao Tong University, Shanghai 200240, PR China*
[b] *School of Mechanical Engineering, Ningxia University, Yinchuan 750021, PR China*
[c] *Department of Mechanical Engineering, Hong Kong Polytechnic University, Hong Kong, PR China*

ARTICLE INFO

Keywords:
Metamaterial
Local resonance
Fault localization
Bandgap tuning
Layer coupling
Spatial encoding

ABSTRACT

To address the challenges of high computational complexity and noise interference in critical equipment vibration localization, this study proposes a novel reconfigurable vibration-encoding methodology based on metamaterial bandgap modulation. By stacking identical resonator units with their masses rigidly connected, elastic deformation arises among the base matrices, forming a coupled configuration in which the overall dynamic response is modified while the intrinsic mass and stiffness of each unit remain unchanged. This approach enables in-situ control of multiple resonators through a single stacking action that induces coupling. Building upon this coupling theory, a tunable encoding metamaterial box (TEMB) is further developed, capable of producing multiple encoding outputs through the coupling of different layers of resonators. Experimental results demonstrate that the TEMB-enhanced diagnosis system enables precise vibration fault localization with a single sensor as the accuracy improves from 87.1% to 97.9% in ten-fold cross-validations. This work realizes bandgap tuning via resonator coupling, breaking the inherent limitations of traditional resonant frequency control methods that exclusively rely on mass or stiffness adjustments. The proposed study introduces the concept of tunable encoding into the vibration transmission encoding and shows promising applications in vibration-based fault detection, while the detachable design philosophy allows for flexible cross-platform deployment.

1. Introduction

Highly symmetrical designs are always desirable in industry [1] for complex mechanical systems with high balancing requirements to increase the range and improve the stability of the system. Taking the helicopter as an example, the drive shaft leading to the tail rotor is symmetrically segmented using identical bearings, ensuring structural uniformity. Nevertheless, this strong symmetry presents inherent challenges: it results in highly similar vibration characteristics and transmission patterns across components, thereby complicating damage localization and fault identification [2]. However, these processes are critical for ensuring system stability [3], reducing equipment failure rates [4], and preventing major accidents [5]. Given the growing emphasis on safety awareness, these issues have attracted significant attention from both industrial and academic communities.

Currently, mainstream techniques rely on deploying multiple measurement points across different locations to perform transfer

---

* Corresponding author.
E-mail address: qbhe@sjtu.edu.cn (Q. He).

https://doi.org/10.1016/j.jsv.2026.119899
Received 11 November 2025; Received in revised form 26 March 2026; Accepted 18 May 2026

path analysis (TPA) [6], cross-correlation analysis [7], and blind source separation [8] on the collected signals. Subsequent feature selection [9] or deep learning model construction [10] is applied to identify potential failures and localize their sources. Feature selection methods correlate fault-sensitive characteristics from both the time domain and the frequency domain with specific failures [11]. In contrast, deep learning models integrate all collected information to derive conclusions, primarily involving techniques such as generative adversarial networks [12], attention-based networks [13], and transfer learning [14]. However, these diagnostic procedures fundamentally rely on discernible variations in output signals, which are often minimized in highly symmetrical systems with severe noise, largely enhancing the localization difficulty. Additionally, the structural spatial configuration and the associated costs at both physical and computational levels continue to present persistent challenges. As a result, there is an urgent need for novel techniques that utilize fewer sensors while achieving higher accuracy, particularly for such complex systems.

Computational sensing methods based on metamaterials offer a useful mean to alleviate these problems [15]. By inserting local resonators into structures like plates [16] or beams [17], artificial periodic structures can be constructed to generate exotic wave propagation properties [18], conducive to controlling elastic waves [19]. As a result, spatial wave encoding of sound and vibration energy can be realized through exploiting various physical mechanisms like Mie resonances [20], phononic crystal cavity resonance [21] and wave compression [22], enpowering classic sensors with the ability of vector measurement. Recently, researchers have developed randomized resonant metamaterials [23], distinctly labeling the waves being transmitted to a single sensor from different locations. By combining compressed sensing and intelligent algorithms such as K-Nearest Neighbor (KNN), it became possible to identify multiple vibration sources by using a single sensor. This technique has also been applied to bearing vibration source identification [24], aircraft skin impact region detection [25], and industrial quadcopter UAV damage localization [26], thus greatly reducing implementation costs and improving detection efficiency, which is highly interesting and practical. Although considerable research has been conducted in this field, specific engineering designs must be developed whenever new requirements for encoding functions arise. This not only makes the design process highly complex but also demands a high level of expertise from engineers.

For the purpose of controlling structure waves in numerous engineering applications, the tunable bandgap methods through resonator designs have been widely exploited [27]. Existing approaches are typically associated with adjusting the mass or stiffness of resonators through origami techniques [28], magnetic force [29], and smart materials [30]. For example, Damiano Pasini [31] et al. developed a reprogrammable rigid origami technique widely used in actuators, robots, and other fields. Bilal et al. [32] demonstrated a phononic transistor-like device through a magnetically coupling method. Li et al. [33] reported on a stimuli-responsive programming effect utilizing shape memory that can sense and control wave propagation when they are either separated or combined together. These researches enable the flexible selection of desired vibration characteristics [34], thereby substantially improving device integration [35] and establishing a robust foundation for tunable vector measurement. However, all the aforementioned methods rely on altering resonant frequencies though mass or stiffness adjustment, applied to each resonator individually.

In this study, a resonator layer-coupling methodology (RLCM) is proposed, where rigidly connected resonator masses and elastically linked bases form dynamic coupling structures with lower resonant frequency under identical parameters. The theoretical, simulation, and experimental results demonstrate a lower resonant frequency after coupling, thus verifying the modifying effect of the vibration properties. The RLCM dynamic model represents an innovative approach, where the coupling between different layers works, rather than variations in stiffness or mass elements, allowing for simultaneous tuning of vibration property for multiple resonators. Then, different layers of resonators are integrated in a transfer encoding metamaterial box (TEMB), with reprogrammable properties given by adaptable combination. An experiment on a rotating mechanical system is conducted to demonstrate the efficacy of the proposed technique. All these make it possible to control the vibration properties of multiple resonators in situ, while the proposed tunable coding method greatly simplifies the complexity of metamaterial coding.

The organization of the article is as follows. In Section 2, randomized resonant metamaterials for single sensor identification of

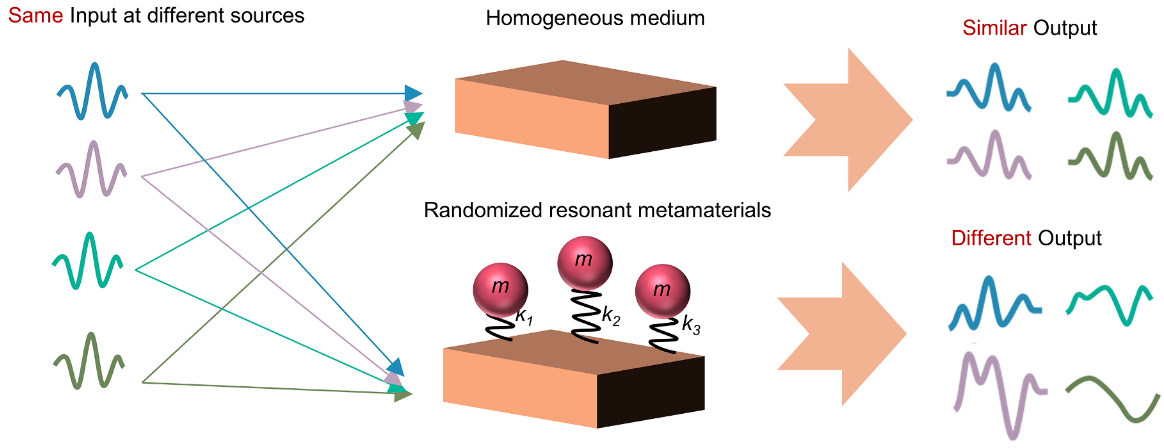

Fig. 1. Spatial filtering effect of random resonance. Top: In a homogeneous medium, the sensor cannot distinguish between similar vibration sources. Bottom: Spectral modulation of vibrations from different locations via randomly coupled resonators enables spatially distinguishable responses at the sensor.

elastic vibrations is introduced, as well as its limitation. In Section 3, the conception of RLCM is proposed for both individual resonators and randomly distributed metastructure design. In Section 4, verification experiments for RLCM are conducted. Then in Section 5, TEMB is first introduced, and an experiment on a rotating mechanical system is conducted to demonstrate its efficacy. Finally, Section 6 discusses the limitation and Section 7 summarizes main conclusions.

2. Theoretical foundation

This section introduces the fundamental concept of the random coupling and randomized resonant metamaterials, which provides the theoretical foundation for encoding spatial information through multiple resonators with distinct vibration characteristics.

In a homogeneous medium, the propagation of acoustic or elastic waves exhibits high spatial symmetry, leading to nearly identical sensor responses to vibrations from different locations. As a result, when multiple vibration sources share similar spectral features, it becomes difficult to distinguish their spatial origins using a single sensor.

To overcome this limitation, resonators with different resonance frequencies can be spatially distributed at various spatial positions, thus vibrations from different locations interact with distinct sets of resonators before reaching the same sensor. As a result, the received signals are modulated by the resonance characteristics corresponding to spatial positions, achieving highly uncorrelated transmission responses that encode spatial information, as illustrated in Fig. 1.

To further illustrate this mechanism, consider a resonant network comprising N local resonators, each of which can be simplified as a frequency-dependent effective mass [23]:

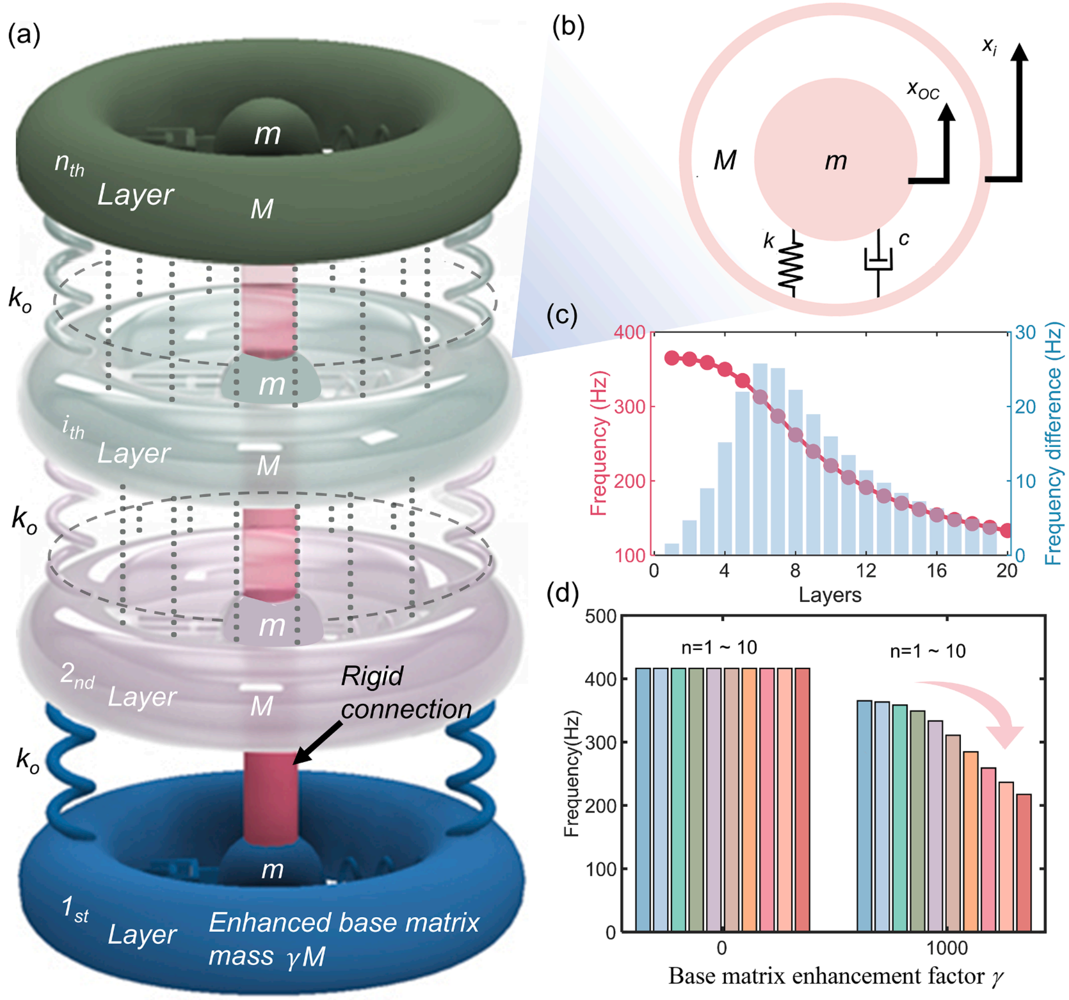

Fig. 2. Stiffness-mass layered coupling model, describing the proposed resonator layer-coupling methodology. (a) Complete coupling architecture where resonator masses are rigidly connected and base matrices are elastically coupled, with the enhanced boundary mass γM at the first layer. (b) Unit layer structure and dynamic variables definition. (c) Relationship between natural frequency and number of coupled layers n, and the frequency difference between consecutive layers configurations. (d) Frequency variation with layer number under different base matrix mass enhancement factors γ.

$$m_n^{eff} = M + \frac{k_n^d m}{k_n^d - \omega^2 m} \tag{1}$$

where $k_n^d = k_n + i\omega c_n$, $k_n = m\omega_n^2$ and ω_n is the resonant frequency of the n-th resonator. Specifically, m represents the real mass of a single resonator, M denote the mass of the matrix and k_n^d corresponds to the stiffness coefficients. The damping term is neglected in the analysis due to its relatively minor influence on the system response. Near the resonant frequency, the effective mass can become negative, corresponding to the attenuation of elastic waves. The overall system can be described as $\mathbf{M}_k^{eff}\ddot{\mathbf{X}}_k + \mathbf{K}_k^c\mathbf{X}_k = \mathbf{F}_k$, where $\mathbf{M}_k^{eff}$ is the global effective mass matrix representing the resonators, $\mathbf{K}_k^c$ is the stiffness coupling matrix describing elastic connections among resonator bases, $\mathbf{X}_k$ is the displacement vector, and $\mathbf{F}_k$ is the external excitation vector.

When all resonators share the same resonant frequency (forming an Ordinary Coupling Network, OCN), the system exhibits a broad attenuation region (bandgap) within the resonant frequency band, which is unfavorable for vibration encoding. However, if the resonant frequencies of the resonators are randomly distributed (forming a Randomized Coupling Network, RCN), the effective mass matrix $\mathbf{M}_k^{eff}$ will become disordered. This disorder leads to highly uncorrelated transmission responses of the system to vibrational inputs from different spatial locations. This disordered coupling mechanism ensures that vibrations with identical spectra, when excited at different locations, produce distinctly different spectral characteristics at the sensor end.

Therefore, random coupling represents a key physical basis for obtaining spatial information about vibrations: it transforms the randomness of coupling into a deterministic encoding of spatial information, enabling efficient vibration source localization with minimal sensing hardware [36].

However, a critical challenge remains: conventional randomized metamaterials require completely new structural designs whenever the encoding function must be updated or altered. This ad-hoc design paradigm not only leads to high complexity in the engineering process but also demands specialized expertise, limiting their adaptability and broader application.

To overcome this limitation, in this study we introduce the resonators layer coupling methodology (RLCM), which shifts the paradigm from designing new structures to reconfiguring existing ones. By enabling in-situ tuning of vibration properties through layer stacking and coupling, our approach bypasses the need for repetitive custom designs.

3. Resonators layer coupling methodology for tunable encoding

To establish the theoretical foundations of tunable encoding mechanisms, this section commences with a systematic exposition of the Resonant Layer coupling methodology (RLCM) and its underlying operational principles. Following this theoretical framework, we employ finite element method (FEM) simulations to quantitatively investigate the spectral shifting capabilities enabled by layer coupling.

Subsequently, Chapter 3.2 introduces a novel reconfigurable vibration transmission encoding model through dynamical analysis and FEM simulation.

3.1. Principle of the resonators layer coupling methodology

Taking a single resonator as an example, the n-layer architecture with replicated component per unit layer can be described as a stiffness-mass model in Fig. 2(a), where the mass of a resonator is represented by m, that of a matrix is simplified as M, and their connections are stiffness element k and damping c. Since the first layer is connected to the test table, it will demonstrate a constraint motion state. In vibration analysis aspect, this boundary condition equals to a higher mass performance on the first layer, thereby correction factor γ is introduced to correct its mass. The resonators m in different layers are assumed to be rigidly linked, whereas the matrices M are connected via elastic springs k_o.

To focus on the intrinsic eigenvalue variation induced by interlayer coupling, damping is omitted in the analytical derivation. The objective of the analytical model is to reveal the layer-dependent frequency reduction mechanism rather than to predict exact resonance values.

Following the standard formulation of linear vibration theory [37], the equations of motion can be expressed as

$$\begin{cases} \gamma M\ddot{x}_1 + k(x_1 - x_{oc}) + k_o(x_1 - x_2) = 0 \\ M\ddot{x}_i + k(x_i - x_{oc}) + k_o(2x_i - x_{i-1} - x_{i+1}) = 0(1 < i \le n) \\ nm\ddot{x}_{oc} + k\sum\limits_{i=1}^{n}(x_{oc} - x_i) = 0 \end{cases} \tag{2}$$

where x_{oc} denotes the resonator displacement, while x_i represents the matrix displacement in the i^{th} layer, as marked in Fig. 2(b). The fixed boundary condition imposes a constrained displacement on x_1, consequently diminishing its dynamic contribution. To establish a unified formulation, we introduce a non-physical parameter x_{n+1} with $x_{n+1} = x_n$. Due to interlayer coupling, total mass of all resonators are collectively expressed as the product $n \times m$.

Assuming a harmonic solution of the form

$$\mathbf{X} = \mathbf{U}e^{i\omega t}, \tag{3}$$

substitution into the equation yields the characteristic equation,

$$\Theta\,\mathbf{U}\overset{\Delta}{=}\left(\mathbf{K}-\omega^2(n)\mathbf{M}\right)\mathbf{U}=\mathbf{0} \tag{4}$$

Here, the stiffness and mass matrices, **K** and **M**, can be concluded as

$$\mathbf{K}=\begin{bmatrix} k+k_o & -k_o & 0 & \cdots & 0 & -k \\ -k_o & k+2k_o & -k_o & \ddots & \vdots & \vdots \\ 0 & -k_o & \ddots & \ddots & 0 & \vdots \\ \vdots & \ddots & \ddots & k+2k_o & -k_o & \vdots \\ 0 & \cdots & 0 & -k_o & k+k_o & -k \\ -k & \cdots & \cdots & \cdots & -k & nk \end{bmatrix}_{(n+1)\times(n+1)}, \tag{5}$$

$$\mathbf{M}=\begin{bmatrix} \gamma M & 0 & \cdots & \cdots & 0 \\ 0 & M & \ddots & & \vdots \\ \vdots & \ddots & \ddots & \ddots & \vdots \\ \vdots & & \ddots & M & 0 \\ 0 & \cdots & \cdots & 0 & nm \end{bmatrix}_{(n+1)\times(n+1)}. \tag{6}$$

Under the proposed framework, $\mathbf{\Theta}$ be expressed as a composite function of ω and n, where the value of $\omega(n)$ itself depends on the layer number n. Subject to the imposed boundary conditions, the characteristic equation admits non-trivial solutions only if

$$\det(\mathbf{\Theta}(\omega))=0, \tag{7}$$

thereby ω can be expressed as a function of layer n and coefficient γ.

To clearly illustrate the theoretical results, we adopt the following parameters from Eq. (7): $m=7.5\times10^{-4}$kg, $M=2.5\times10^{-3}$kg,

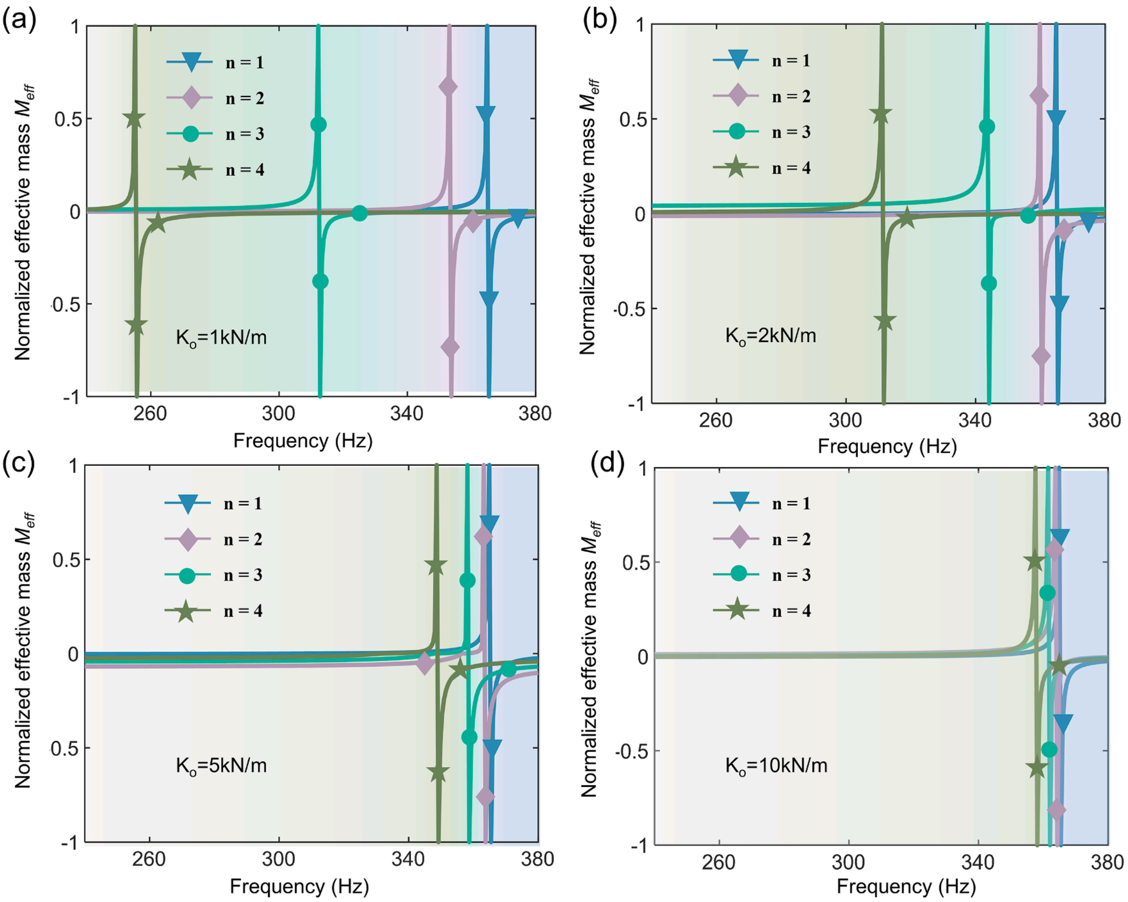

Fig. 3. Variation of the effective mass M_{eff} with frequency for structures comprising one to four layers, under different layer connection stiffness k_o. (a) $k_o=1$ kN /m, (b) $k_o=2$ kN /m, (c) $k_o=5$ kN /m, and (d) $k_o=10$ kN /m.

$k_o = 5 \times 10^3$N/m, and $k = 1 \times 10^2$N/m, with γ first considered infinite to best approximate the absolute fixed boundary condition.

The numerical calculation results performed using MATLAB R2023a are presented in Fig. 2(c). The result shows that the fundamental frequency decreases from 365 Hz to 126 Hz as the number of layers increases from one to twenty, which represents the main variable variation of interest in this study. The bar graph further demonstrates that the frequency difference between adjacent layers progressively increases from single-layer to six-layer configurations, then gradually decreases in magnitude when increasing from six to twenty layers, this behavior is an auxiliary observation beyond the primary focus of the current theoretical analysis.

Then, the influence of coefficient γ is also considered with $\gamma = 1$ and 1000 in Fig. 2(d). As evident from the results, a decreasing trend emerges across all layer numbers when γ reaches an order of magnitude of 10^3. At $\gamma = 1$, the frequency remains constant at 416 Hz regardless of the increase in layers, which corresponds to a free boundary condition at the bottom layer. In this case, the mass matrix remains a scalar matrix, and the coupling effect cannot be activated, indicating that the proposed method requires the base layer to be fixed to take effect.

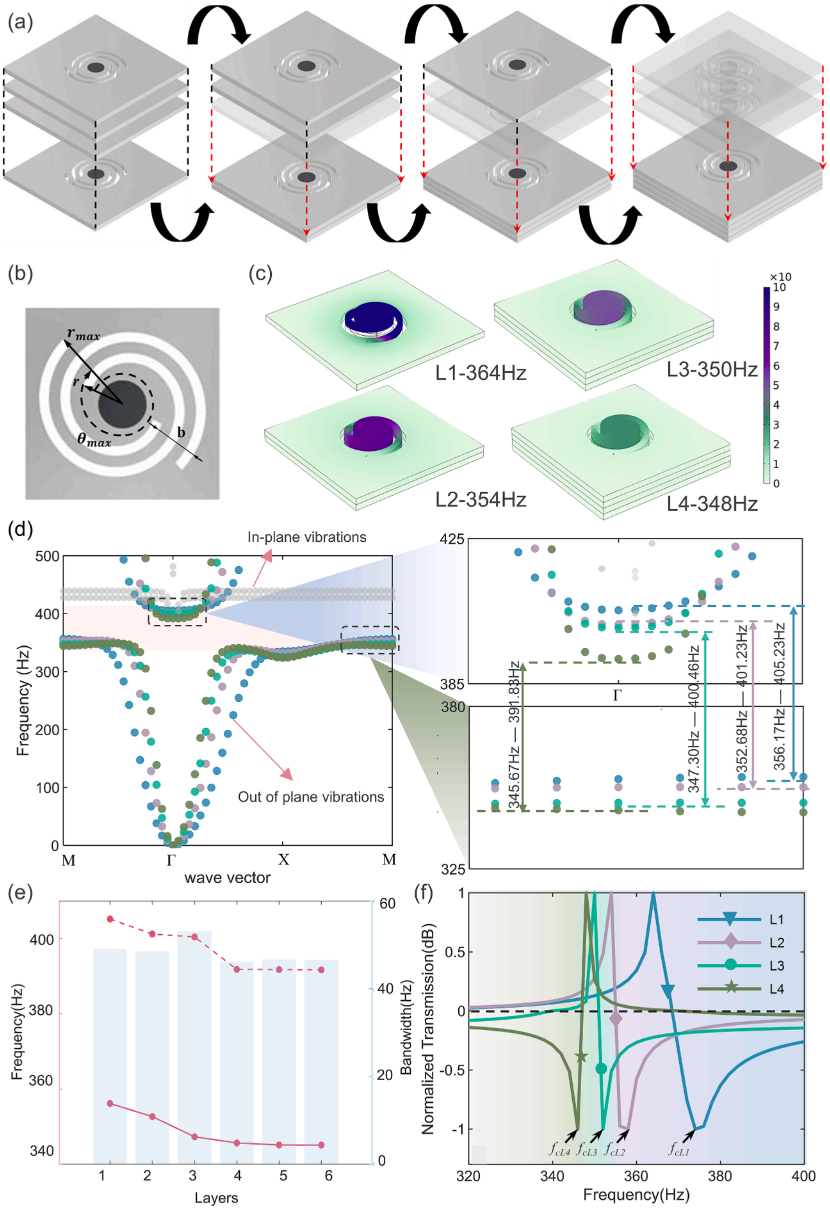

Fig. 4. Realization and FEM validation of the resonator layer coupling effect. (a) Schematic of the layer coupling process. (b) Vertical view of a resonator. (c) First-order vibration modes and their frequency for different layers, color bars represent the vibration amplitude. (d) The band structure of different layers configuration across the entire Brillouin zone, edge detail presented on the right. (e) Bandgap analysis. The line graph shows the upper and lower edges of the bandgap, while the bar graph represents the bandwidth. (f) Normalized transmission variation.

To better understand the variation in vibration characteristics, it is instructive to introduce an excitation in the matrix of the base layer. After performing the Laplace transform and subsequent processing, we obtain the excited displacement as:

$$\mathbf{X} = \mathbf{F}/\left(s^2\mathbf{M} + \mathbf{K}\right). \tag{8}$$

Here, $s = i\omega$ is the complex frequency variable, $\mathbf{X}(\mathrm{s}) = \mathscr{L}(\mathbf{x}(\mathrm{t}))$ and $\mathbf{F}(\mathrm{s}) = \mathscr{L}(\mathbf{f}(\mathrm{t}))$ denote the Laplace transforms of the displacement vector $\mathbf{x}(\mathrm{t})$ and the force vector $\mathbf{f}(\mathrm{t})$, respectively, where the force vector $\mathbf{f}(\mathrm{t})$ is defined as:

$$\mathbf{f}(t) = [f_s \quad 0 \quad \ldots\ldots \quad 0]^T, \tag{9}$$

where $f_s = 1$ represents a unit input force.

Then, for an n-layer structure, the effective mass model M_{neff} can be derived as

$$M_{neff} = -\frac{f_s}{\omega^2 x_1}. \tag{10}$$

The analysis adopts the following parameters in Eqs. (7) and (9): $m = 7.5 \times 10^{-4}$kg, $M = 2.5 \times 10^{-3}$kg, $k = 1 \times 10^2$N/m and $\gamma = 50$. Fig. 3 presents the layer-dependent behavior of M_{neff} under varying interlayer stiffness $\mathrm{k_o}$ (one layer to four layers configuration selected for analysis).

A distinct trend emerges where the minimum values of M_{eff} progressively shift toward lower frequency ranges as the coupling layer quantity n increases. Consequently, elastic waves propagating through the metastructure exhibit frequency-dependent enhancement or suppression modulated by the layered coupling configuration. This frequency selective character validates the efficacy of the proposed RLCM in bandgap regulation.

The implementation of the proposed stiffness–mass coupling model is illustrated in Fig. 4(a), which demonstrates the progressive coupling sequence of a four-layer resonator system. The coupling is realized by rigidly connecting the resonator masses, which induces elastic deformation in the base matrices between adjacent layers. In this way, identical resonator units are combined into a coupled configuration without altering the intrinsic mass or stiffness of each unit. To achieve this rigid connection in practice, neodymium-iron-boron (NdFeB) permanent magnets are employed, although other detachable connection methods could also be used.

Each individual supercell, as shown in the vertical view in Fig. 4(b), consists of a polylactic acid (PLA) designed matrix, two spiral beams, and a circular NdFeB magnet. The thickness of both the matrix and the magnet is $h = 1.25$ mm, and the descriptive equation of the spiral beams are

$$\begin{cases} x(\theta) = \left(r + \dfrac{b\theta}{2\pi}\right)\cos\theta \\ y(\theta) = \left(r + \dfrac{b\theta}{2\pi}\right)\sin\theta \end{cases}. \tag{11}$$

Here, r represents the distance from the center of the spiral to its starting point, b means the increasing radius corresponding to per growing turns while θ vary from 0 to $\theta_{\max}$ controls the turns of the spiral. For each supercell, there is a unique $\theta_{\max}$ which reflects the stiffness of the cell.

Use COMSOL Multiphysics 5.6 for finite element analysis. Here, supercell with $\theta_{\max} = 2.12\pi$ is selected firstly, material parameters of which are set as: Young's modulus $E_{\mathrm{PLA}} = 2.636$ Gpa, Poisson's Ratio $\upsilon_{\mathrm{PLA}} = 0.41$, and Density $\rho_{\mathrm{PLA}} = 1170\mathrm{kg/m^3}$ for PLA matrix while $E_{\mathrm{NdFeB}} = 150$ Gpa, Poisson's Ratio $\upsilon_{\mathrm{NdFeB}} = 0.24$, and Density $\rho_{\mathrm{NdFeB}} = 7800\mathrm{kg/m^3}$ for NdFeB magnet.

Generally speaking, the formation of bandgaps can be attributed to factors such as out-of-plane vibrations, in-plane vibrations, and torsional vibrations. Among them, the out-of-plane mode is often utilized due to its characteristic as a first-order mode and its ability to control the bending waves. So, the out-of-plane vibration modes are here taken for analysis as an example.

The FEM results of one to four layers in Fig. 4(c) reveal the changes in vibration states through the coupling process. It is clear that resonant frequencies gradually decrease and vibration peaks progressively diminish as the number of layers increases. This trend turns less obvious as the layers involved in the model increase.

Further band structure analysis under periodic conditions is conducted, with the results presented in Fig. 4(d) and Fig. 4(e).

As depicted in Fig. 4(d), when the number of coupled layers increases from one to four, the edge detail clearly demonstrates a decrease in the bandgap frequency from 356.17 to 405.23 Hz to 345.97–391.83 Hz. It is also obvious in Fig. 4(e) that the bandwidth of the bandgap is almost unaffected by the coupling variation.

As for transfer function aspect, that from the left side to the right side of the cell is defined as $T = 20\log\left(\frac{P_{out}}{P_{in}}\right)$, where P_{out} means the measured value of the acceleration at the output, P_{in} refers to that at the input. The relation between normalized transmission and frequencies is shown in Fig. 4(f). The frequencies corresponding to the maximum attenuation within each bandgap, denoted as $\mathrm{f_{cL1}}$–$\mathrm{f_{cL4}}$, are marked to indicate the core attenuation frequencies of the bandgaps for different layer configurations. It is evident that the core frequency of the bandgap exhibits a systematic leftward shift as the layer number increases, consistent with the reduction in resonant frequency.

For validating the effectiveness of this principle across a wide range, situations of different spiral beam parameters are also discussed in Fig. 5. Specifically, Fig. 5(a–d) present the variation in natural frequency with respect to the max spiral angle $\theta_{\max}$, increasing radius coefficient b, resonator radius r, and single-layer height h, respectively. In all cases, the comparison across one to four layers shows a consistent trend in which the natural frequency decreases with increasing layer number, thereby supporting the universality of the frequency-reduction mechanism induced by layer coupling.

3.2. *Tunable vibration transmission encoding*

Section 3.1 introduces a method for in-situ tuning of resonator vibration properties through layer coupling. In this section, the effect of RLCM in coordinated tuning of multiple resonators will be demonstrated. As an application, such synchronized control of vibration characteristics can be employed to realize tunable encoding, which introduces spatially randomized vibration responses within an otherwise homogeneous medium.

Here, to demonstrate the aforementioned effect, the tunable effective mass unit in Section 3.1 is introduced as a supercell, whose effective mass varies along with layers. All the supercells are connected through stiffness and damping elements in series in Fig. 6(a).

For the resonators system, from Newton's second law and Hook's law, the dynamic equation can be written as:

$$\begin{cases} m_{effi}\ddot{x}_j + c_w\left(\dot{x}_j - \dot{x}_{j+1}\right) + k_w\left(x_j - x_{j+1}\right) = 0 & (j = 1) \\ m_{effi}\ddot{x}_j + c_w\left(2\dot{x}_j - \dot{x}_{j-1} - \dot{x}_{j+1}\right) + k_w\left(2x_j - x_{j-1} - x_{j+1}\right) = 0 & (1 < j < m) \\ m_{effi}\ddot{x}_j + c_w\left(\dot{x}_j - \dot{x}_{j+1}\right) + k_w\left(x_j - x_{j+1}\right) = 0 & (j = m) \end{cases}. \tag{12}$$

Respectively, the Laplace transform of Eqs. (12) are

$$\begin{cases} m_{effi}s^2X_i + c_w s\left(X_j - X_{j+1}\right) + k_w\left(X_j - X_{j+1}\right) = 0 & (j = 1) \\ m_{effi}s^2X_j + c_w s\left(2X_j - X_{j-1} - X_{j+1}\right) + k_w\left(2X_j - X_{j-1} - X_{j+1}\right) = 0 & (1 < j < m) \\ m_{effi}s^2X_j + c_w s\left(X_j - X_{j-1}\right) + k_w\left(X_j - X_{j-1}\right) = 0 & (j = m) \end{cases}. \tag{13}$$

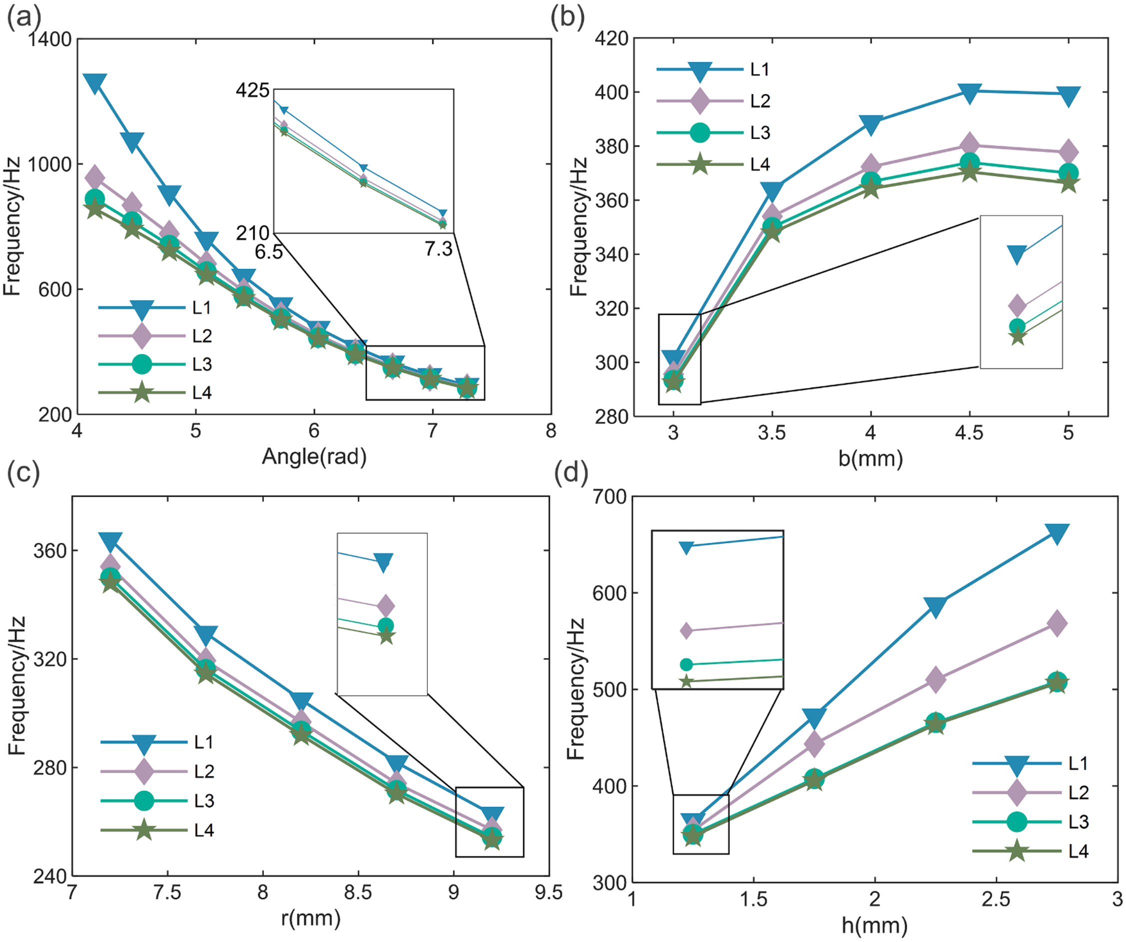

Fig. 5. The influence of the spiral beam parameters on natural frequency involving single layer to four layers configuration. (a) Spiral angle θ. (b) Increasing radius coefficient of spiral beam b (c) Resonator radius r (d) Height of one layer h.

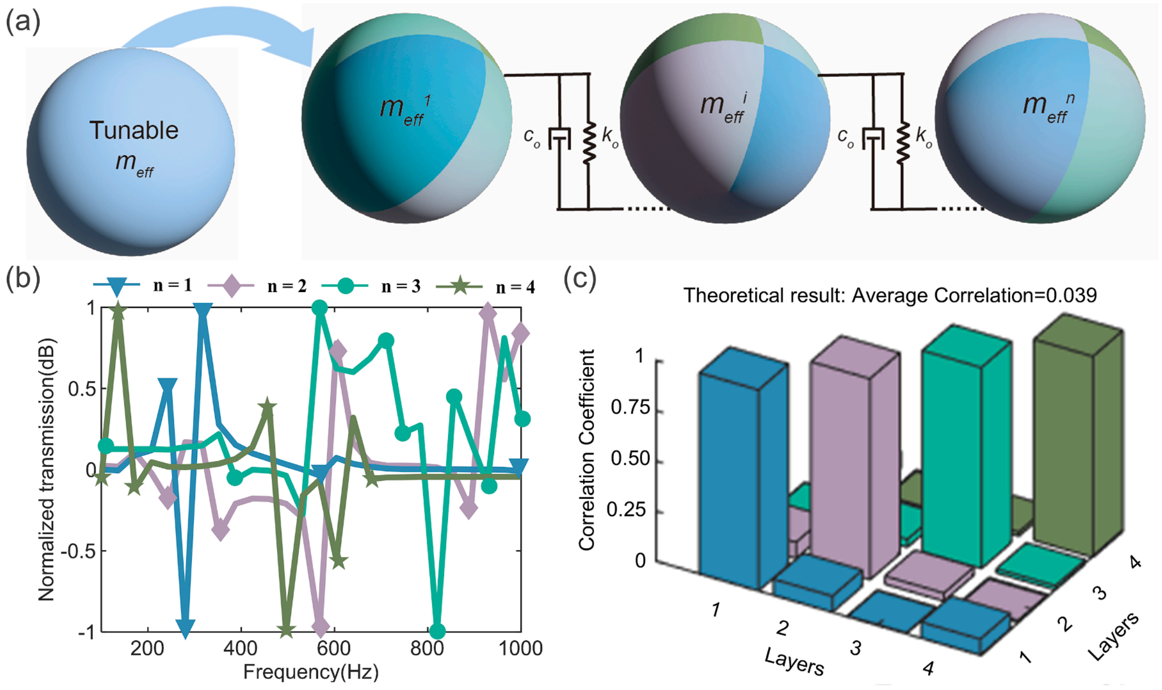

Fig. 6. Layer-coupling-mediated transmission variation model. (a) Resonator system composed of layers-dependent effective mass, connected via stiffness k_o and damping c_o. (b) Highly uncorrelated transmission characteristics across different numbers of coupled layers. (c) Theoretical cross-correlation coefficients, with an average value of 0.039.

For a definite coupling result, vibration transmission between adjacent resonators can be described by

$$T_j = \frac{X_{j+1}}{X_j}. \tag{14}$$

From Eqs. (14) and (15), we obtain

$$T_j = \begin{cases} \dfrac{m_{effj}s^2 + c_w s + k_w}{c_w s + k_w} & (j = 1) \\ \dfrac{\left(m_{effj}s^2 + 2c_w s + 2k_w\right)T_{j-1} - c_w s - k_w}{m_{eff(j-1)}s^2 + c_w s + k_w} & (1 < j < m-1) \\ \dfrac{c_w s + k_w}{m_{eff(j+1)}s^2 + c_w s + k_w} & (j = m-1) \end{cases}. \tag{15}$$

Then, the transmission of the system can be described as

$$T = \frac{X_n}{X_1} = T_1 T_2 \cdots T_j \cdots T_{n-1}. \tag{16}$$

Since T_1, T_2, …, T_n are pairwise coprime, T must be a function of $\mathrm{m}_{\mathrm{eff1}}$, $\mathrm{m}_{\mathrm{eff2}}$, …, m_{effn}, where the coefficient of m_{effj} must not be zero. The change in the effective masses results in a different transfer function, which inevitably occurs once coupling takes place. Then, for the same input wave, the output vibration varies due to the differences in transmission. By utilizing the output data and the system characteristics, which are already known when designing, the input vibration can be back-calculated, thereby forming a position encoding of the vibration information.

To provide visual evidence, numerical simulations were conducted in MATLAB, and the results are presented in Fig. 6(b) and (c). The simulation parameters are set as follows: the mass of the resonator $m = 7.5 \times 10^{-4}$ kg, the mass of the main structure $M = 2.5 \times 10^{-3}$ kg, the coupling stiffness $k_o = 5 \times 10^3$ N/m and correction factor $\gamma = 50$. Six different connection stiffness k corresponding to the spiral angle θ are randomly generated within the range of 200–1200 N/m. Fig. 6(b) shows the resulting normalized transmission spectra calculated based on Eq. (16), while Fig. 6(c) presents the corresponding cross-correlation coefficients between multilayer configurations. The average correlation coefficient is approximately 0.039, indicating low spectral similarity among the transmission profiles under different coupling conditions.

Fig. 7(a) demonstrates the realization of a tunable encoding process, where four plates, each embedded with six local resonators of different effective masses, can be either separated or stacked together. Each supercell maintains identical constituents to Fig. 4(b) but different geometry values. As shown in Fig. 7(b), the FEM modal analysis indicates that increasing the number of layers reduces the natural frequency of the first-order out-of-plane vibration mode of each resonator. For clarity, the corresponding frequencies under one-to-four-layer configurations are denoted as f_{L1}, f_{L2}, f_{L3}, and f_{L4}. The integrated bar chart in Fig. 7(b) then quantitatively illustrates the interlayer frequency differences. Subsequently, the transmission characteristics of the metastructure with 1 to 4 layers are obtained by defining input and output probes at appropriate positions in the finite element model. The result in Fig. 7(c) exhibits a chaotic distribution across the frequency band of 100Hz-1000 Hz. This phenomenon can be demonstrated by the correlation coefficient defined as

$$Corxy = \frac{\sum_{p}\left[T_x(\omega_p) - \overline{T}_x\right]\left[T_y(\omega_p) - \overline{T}_y\right]}{\sqrt{\sum_{p}\left(T_x(\omega_p) - \overline{T}_x\right)^2}\sqrt{\sum_{p}\left(T_y(\omega_p) - \overline{T}_y\right)^2}}. \tag{17}$$

With the coefficient $Corxy = 0.1594$ between these four transmissions in Fig. 7(d), the multiple resonantors tuning capacity as well as the encoding ability of RLCM are proved. The emergence of this capability means that different spatial filtering results can be obtained simply by using different layers of structure.

4. Experimental verification

In this section, the performance of RLCM will be measured through a vibration exciter sweep frequency experiment. In Section 4.1, the setup of the experiment system will be first demonstrated with its workflow. Then, both the gain factor of the first-order natural frequency for a supercell and the transmission of the metastructures with random distributed resonators will be chosen for the experiment whose results will be shown in Section 4.2.

4.1. Experimental setup

Fig. 8 demonstrates the setup of the experimental system to verify the performance of the metastructure. In Fig. 8(a), the working flow chart of the experimental equipment is clearly described. The sweep frequency signal is generated by the signal generator (SDG2122X), amplified by the power amplifier (YE5872A), and then input into the test element using the exciter (B&K 4808). Since the excitation direction is parallel to the plate thickness direction, we can only capture vibration information corresponding to out-of-plane modes. The tested structure includes a fixed plate and metastructures full of resonators, with the edge of the metastructure at

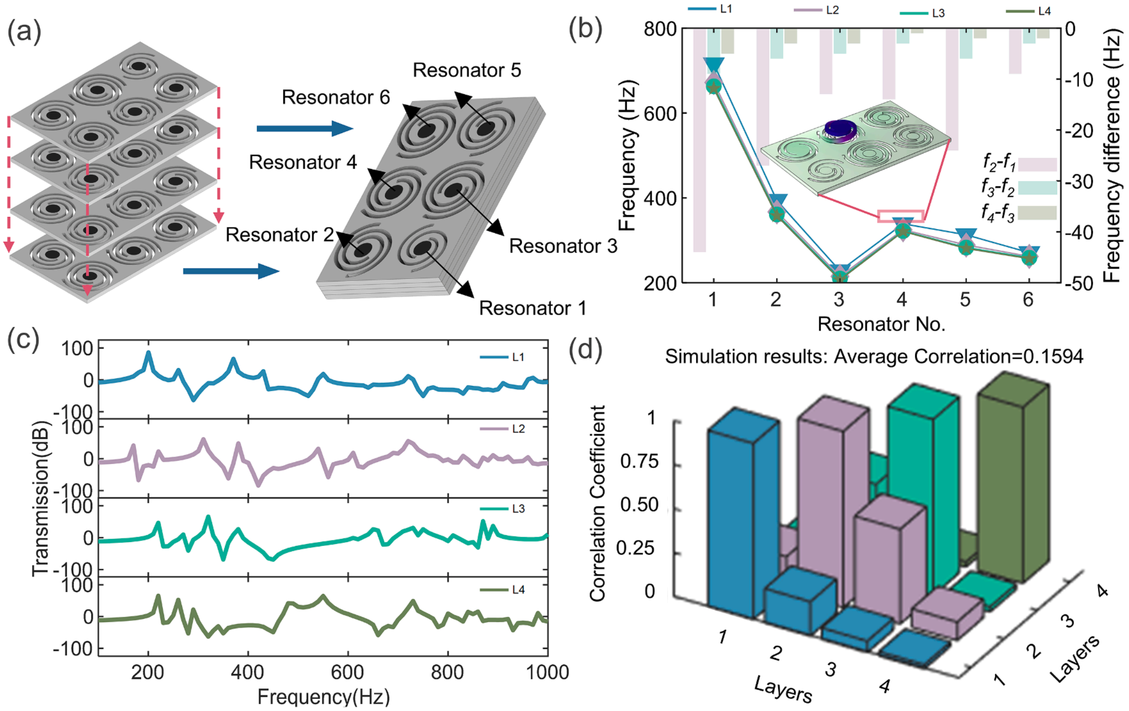

Fig. 7. FEM randomly distributed layer coupled model. (a) Schematic of the randomly distributed layer-coupled structure and resonator numbering. (b) Natural frequencies of the first-order out-of-plane vibration mode of each resonator for configurations with one to four layers, the frequency differences are illustrated by bars. (c) Normalized transmission comparison between one to four layers configurations. (d) Simulation cross-correlation coefficients, with an average value of 0.1594.

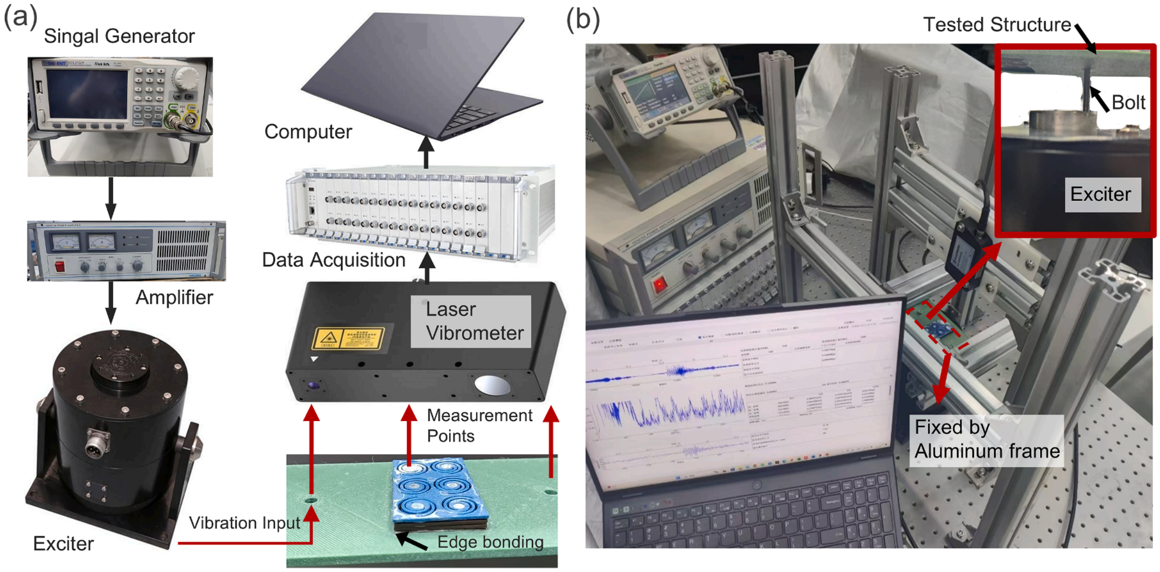

Fig. 8. Experimental system setup. (a) Schematic of the system composition and workflow: The exciter, driven by a signal generator and amplifier, induces vibrations that are modulated by the metastructures. The vibration response is measured using a laser vibrometer and transmitted to a computer via a data acquisition system for analysis. (b) Photograph of the experimental setup, showing the metastructures securely bolted to the exciter.

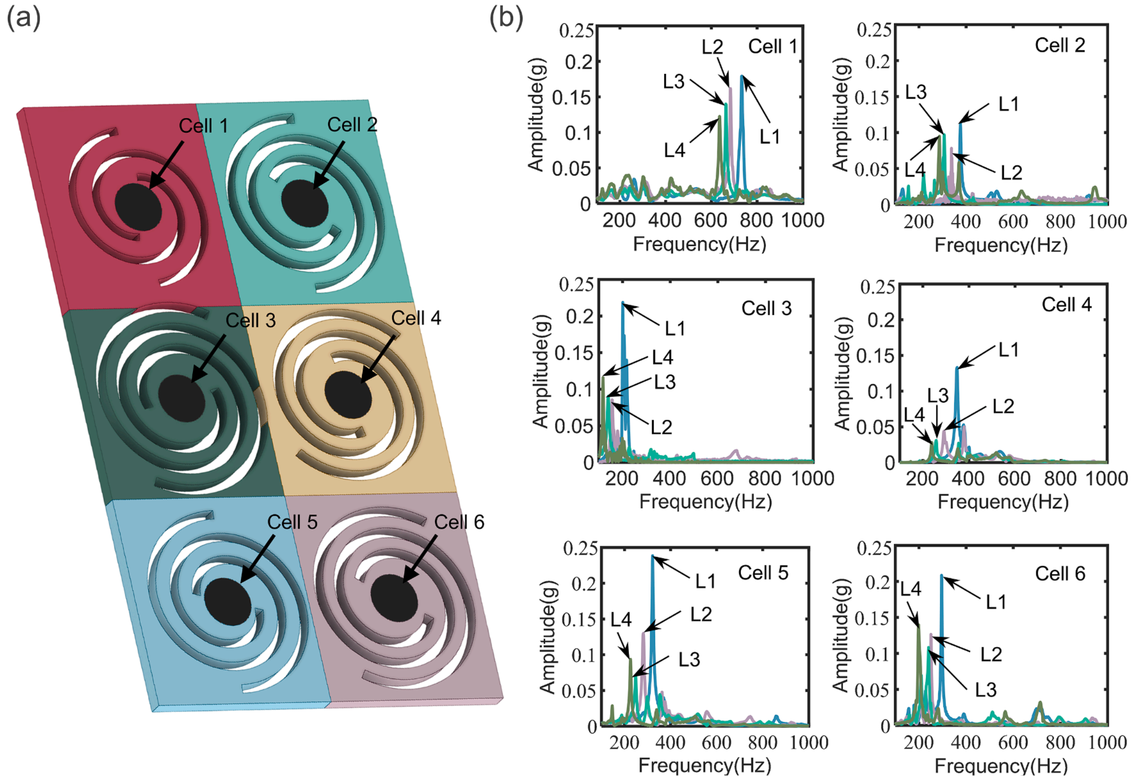

Fig. 9. Experimental verification results of RLCM. (a) Tested structures, with the laser measurement point positioned at the center of each cell; different colors indicate different cells. (b) Gain factors of all six resonators across varying layer numbers, showing a decreasing trend in frequency as the number of layers increases, confirming that the RLCM is applicable to each individual resonator.

the bottom connected to the fixed plate by adhesive. The fixed plate is secured to the aluminum test bench using four bolts. Here, both the fixed plate and metastructure are made by 3D laser printing with PLA material. A cavity in the center of each supercell is pre-drilled for inserting magnets.

The vibration signal generated by the exciter is input on the left of the plate through a bolt while the output of the metastructure is considered on the right hand. The input, local resonance, and output vibration information are collected separately using a laser vibrometer (Kathmatic). Then, the collected signal is transmitted to the computer via data acquisition (DH8300N). The whole system is located on the isolation platform through the aluminum profile. The photograph of the testing system is shown in Fig. 8(b).

4.2. Test for vibration performance verification

Firstly, the metastructure shown in Fig. 9(a) is set on the test platform. The centers of the resonators are selected for the laser measurement point, with 1 to 4 layers picked for research. In this measurement strategy, the acceleration amplitude of different layers will be demonstrated on the frequency domain, thus the natural frequency will be easily acquired. Here, the sweep frequency period is set to 1 s, and the sweep frequency band is 100Hz-1000 Hz. The frequency-domain test result within the range of 100–1000 Hz is shown in Fig. 9(b) after FFT processing.

Taking cell 1 as an example, frequencies of one layer to four layers are respectively 733 Hz, 684 Hz, 663 Hz and 635 Hz. The result demonstrated a clearly frequency decrease with each layer involved in coupling. The testing trend generally agrees with that predicted by theoretical analysis and FEM simulation, although the magnitude of the frequency shift differs between the FEM and experimental results. This discrepancy mainly arises from the neglect of nonlinear contact interactions across stiffness elements in the FEM model. Nevertheless, the consistent decreasing trend verifies the effectiveness of the proposed RLCM at the experimental level. The detailed comparison between the simulation and experimental results is provided in Appendix A.

Notably, since the experimental system inherently involves material and structural damping, the consistency of the frequency reduction trend further confirms that the coupling-induced mechanism remains valid under practical damping conditions.

To ensure comprehensive validation, measurement results from other cells are also considered. The effectiveness of the RLCM is consistently observed across different resonators whose uncoupled fundamental frequencies span the range of 200 Hz to 800 Hz. This wide operational bandwidth establishes a foundation for subsequent tunable encoding capability tests.

Then, the output information, as well as the transmission of the system, are selected for research. The sweep frequency period is also set to 1 s, and the sweep frequency band is also 100Hz-1000 Hz. As shown in Fig. 10(a), each distinct output peak around 200 Hz,

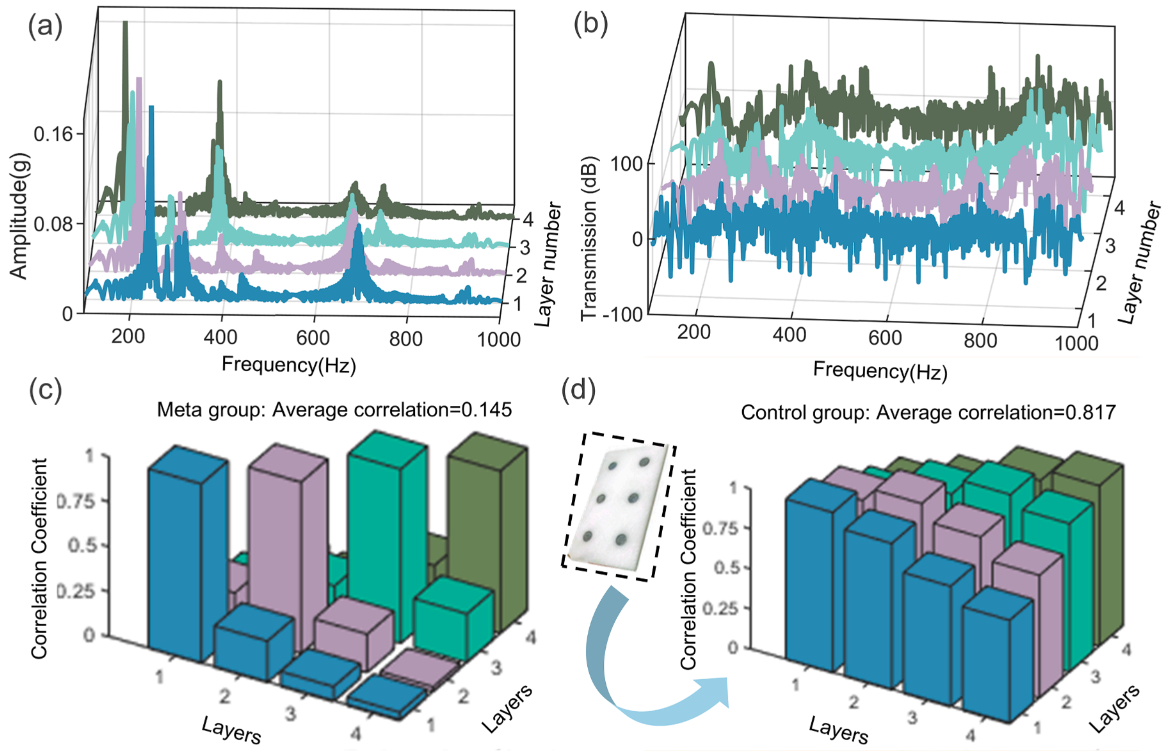

Fig. 10. Performance verification experiment results. (a) Output signal of the metastructures, exhibiting clear frequency tuning. (b) Highly uncorrelated transmission characteristics across different numbers of coupled layers. (c) Cross-correlation coefficients between the transmission responses of the metastructure under different layer configurations, with an average value of 0.145. (d) Cross-correlation coefficients for the control structure without resonators, with an average value of 0.817.

400 Hz, and 700 Hz shifts toward lower frequencies when coupling occurs, indicating a coupling-induced modification of the vibration response. These frequency shifts lead to variations in the transfer function, resulting in the highly uncorrelated transmission characteristics observed in Fig. 10(b). The quantitative analysis in Fig. 10(c) shows a clear discrepancy in transmission, with an average cross-correlation coefficient of 0.145. This transmission characteristic enables waves passing through different layers to be encoded in completely different ways. In contrast, the control test using a board without resonators, shown in Fig. 10(d), but also magnetically attached, yielded a average transfer function correlation as high as 0.817. This comparison further confirms the feasibility of adjustable encoding through RLCM.

Considering that, under practical operating conditions, most encoding scenarios are subject to fluctuating rather than stable inputs, it is essential to evaluate the robustness of the encoding performance against variations in input amplitude. For nonlinear testing, Fig. 11 examines input excitation amplitudes of 100 mV, 200 mV, and 500 mV, with the gain of the power amplifier kept constant. It is obvious in Fig. 11(a) that the corresponding cross-correlation coefficients have an average value of 0.145, 0.187, and 0.157 for the 100 mV, 200 mV, and 500 mV cases, respectively. While Fig. 11(b) shows that the correlation coefficients between different input amplitude situations under identical layers are 0.738, 0.853, 0.725, and 0.635, which are much higher than those between different layers.

What's more, Fig. 11(c) further compares the correlations between different voltages with the same layers and different layers with the same voltage. It can be observed that high correlation persists under identical layers despite varying excitation amplitudes, whereas low correlation is maintained across different layers. This clear distinction indicates that variations in input amplitude have little influence on the encoding results, thereby confirming the robustness of the proposed approach under non-ideal operating conditions.

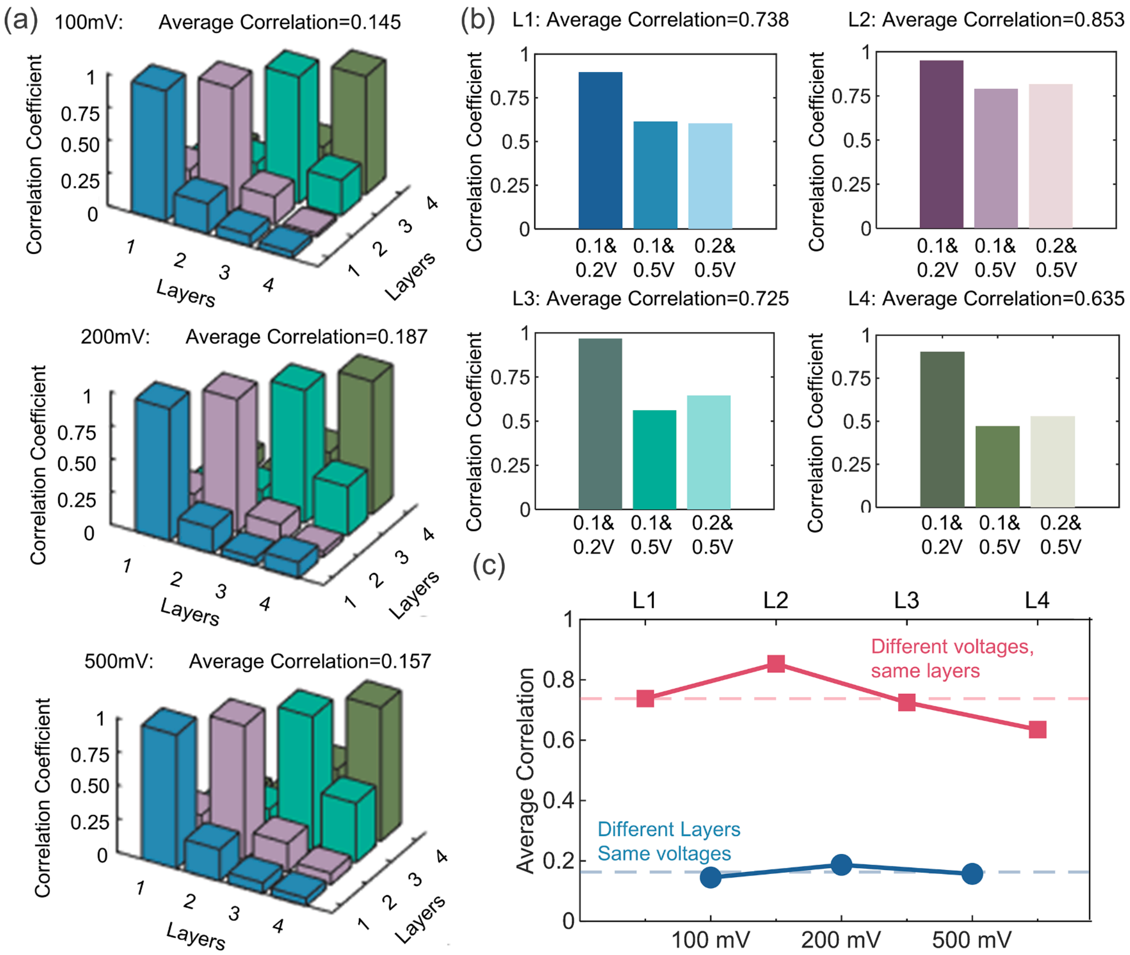

Fig. 11. Encoding robustness analysis under input amplitudes of 100 mV, 200 mV, and 500 mV. (a) Cross-correlation coefficients across different layers under varying input amplitudes, yielding average values of 0.145, 0.187, and 0.157 for 100 mV, 200 mV, and 500 mV, respectively. (b) Cross-correlation coefficients for identical layer numbers under different input amplitudes. (c) Comparison between different voltages with the same layers and different layers with the same voltage, demonstrating that outputs under different layers remain lowly correlated, while outputs under identical layers remain highly correlated even with varying excitation amplitudes.

5. Application in bearing fault vibration localization

In this section, to highlight the advantages of RLCM, four layers of resonators will be integrated tightly in a tunable encoding metamaterial box (TEMB). Its application in assisting bearing fault localization with a single sensor will also be shown. The organization of this section is as follows: the composition of TEMB will be first presented in Section 5.1, followed by its insertion into a rotating machinery system for experimental validation. Then, a detailed description of the experimental system will be provided along with an explanation of the localization principle. In Section 5.2, the effect of TEMBs will be demonstrated through a visible level. Finally, the fault localization analysis based on K-Nearest Neighbor (KNN) is conducted. The results show that the method we propose can significantly improve fault identification accuracy with a single sensor, while the design cost will be extremely low.

5.1. Experimental prototype and setup

The main body of the TEMB is a compact box whose dimensions are 650 mm in length, 650 mm in width, and 300 mm high, as shown in Fig. 12(a). Within the exploded view of the TEMB in Fig. 12(b), four metasturctures same as that one in Fig. 9(a) are used for encoding, with one of them fixed on the subject by bolt and magnetically attached to others. Every single plate except the one at the bottom can be moved to the top of the box because of the existence of the cube magnet, thus giving it the ability to meet different demands in encoding.

In principle, a single TEMB can be configured in three distinct coupling arrangements: 4 layers and 0 layers, 3 layers and 1 layer, and 2 layers and 2 layers, resulting in three different encoding effects. Since the output of the unencoded structure differs from all three, a four-layer TEMB can therefore be employed to encode four identical structures. Of course, this serves merely as an illustrative example; in principle, a greater number of TEMB layers could be employed to achieve a larger number of encoding possibilities.

For verifying the effect of TEMB, Fig. 13(a) set up a rotary mechanical system consisting of a driving motor, two load motors, a shaft carrying four identical bearings, a gearbox, and other components. For the sake of clarity, these bearings will be referred to as bearing 1 through bearing 4, from right to left. All the signals are collected via an accelerometer positioned on the bearing housing of bearing 1 and transmitted back to the computer through data acquisition.

Here, three TEMBs were positioned on the bearing house of bearing 2 to bearing 4 serving as the experiment group (EG) as is shown in Fig. 13(b), while a parallel configuration without TEMBs serves as the control group (CG). Each TEMB adopted a different layer-coupling configuration to realize tunable encoding: one with 1 layer below and 3 layers above, one with 2 layers below and 2 layers above, and one with 3 layers below and 1 layer above. The configurations were fixed during testing, and mechanical integration between the TEMBs and the system was achieved using bolts. An outer ring fault is introduced sequentially into each bearing, with the cracks illustrated in Fig. 13(c) and the corresponding spectra (700RPM situation) shown in Fig. 13(d).

Since all the bearings are identical, the fault frequency as well as the waveform collected would also be similar no matter where the fault bearing is located. When the system has been pre-encoded, as the coupling effect shown in Fig. 10, the signals at the output end will differ due to the spatial filtering processes, even if their input information is identical. Thereby, the system is enabled to be classified by the algorithm.

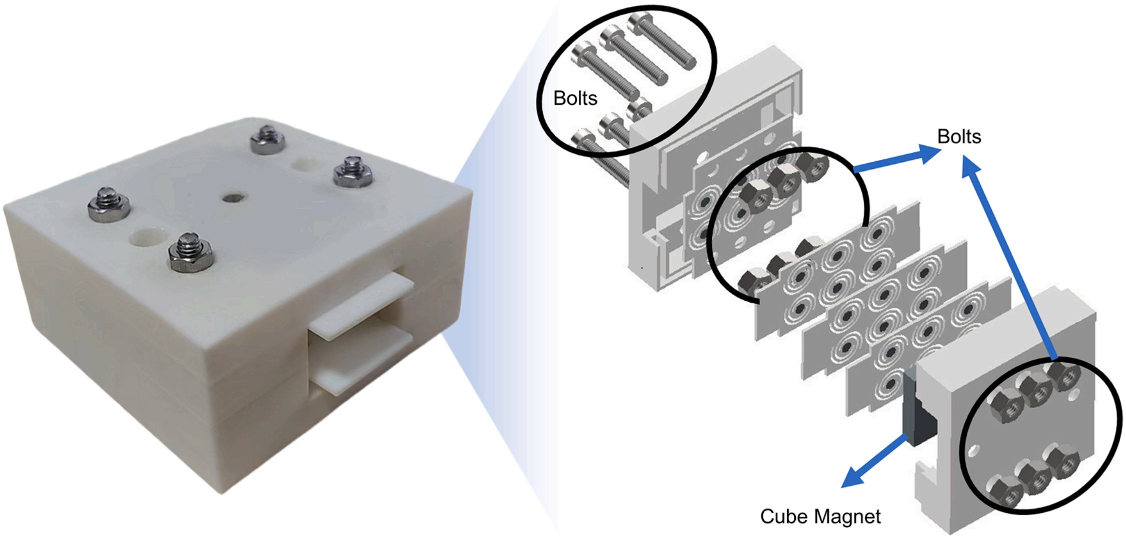

Fig. 12. Structure of TEMB.

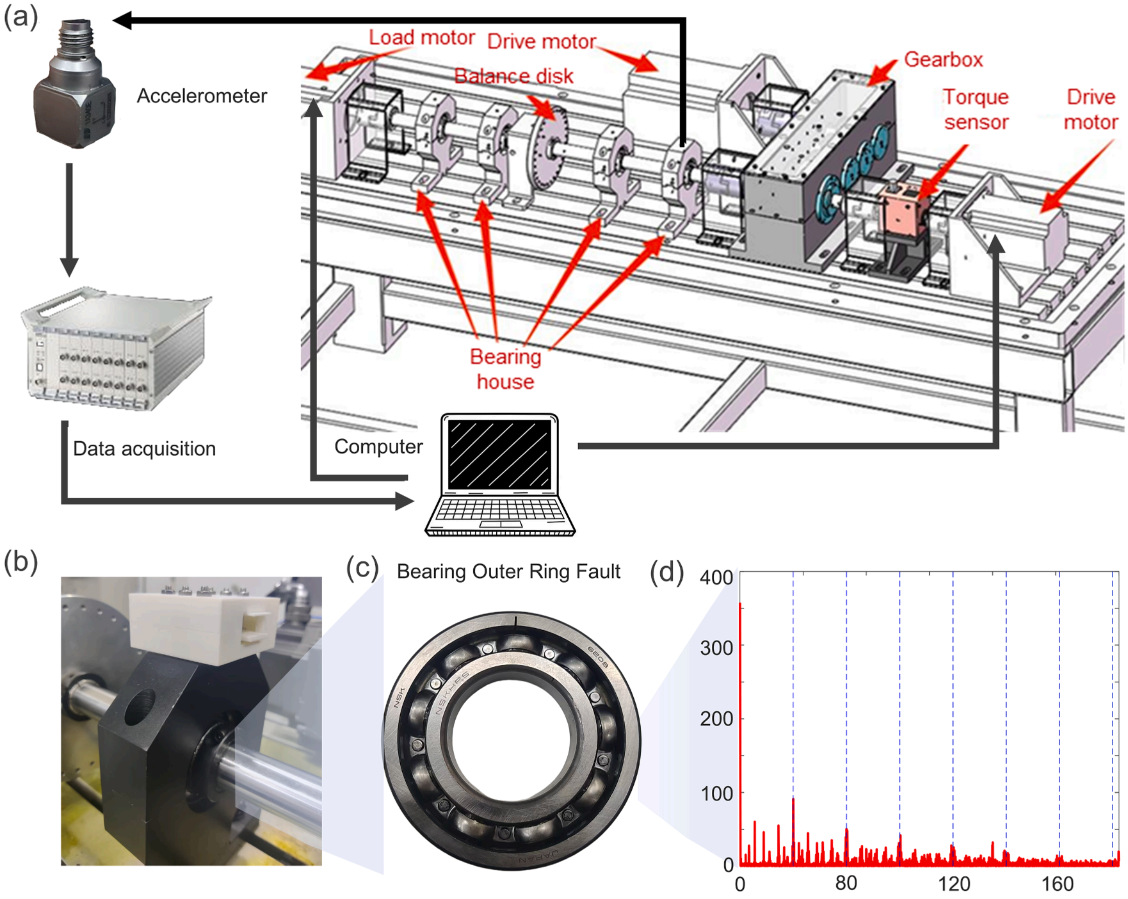

Fig. 13. The rotary mechanical system and identification principle. (a) from the rotary system are captured by an accelerometer and transmitted to a computer via data acquisition. (b) TEMBs are positioned above the bearing housing and secured with a bolt. (c) Outer-ring-fault bearing with a 2 mm crack and (d) its corresponding vibration characteristics.

5.2. Fault localization results

Defining the setting the speed of the drive motor to 700 RPM and collecting the signal with different fault localization respectively, the correlation coefficient of the spectrums is shown in Fig. 14(a) and Fig. 14(b). It is obvious that there would be a lower value for the result with TEMB (0.36) than that without TEMB (0.60), verifying the encoding effect in giving differences to the fault characteristics during transmission.

Furthermore, the spectral components were selected as classification features. In the collected data, we extract the spectrum of each 1-second interval as a sample, thereby constructing a sample set consisting of 240 samples in 4 classes. For visualization purposes, Principal Component Analysis (PCA) was employed to reduce the dimensionality of the samples to two dimensions. The results of the control group in Fig. 14(c) show the principal components of the frequency spectrum. It is clear that they are aliased with each other, especially when the fault is located in the second or third bearing. While it is clearly separated from each other after TEMB is introduced into the system, as is shown in Fig. 14(d). Here, points representing fault 1 are clearly separated from other points, which means that the accelerometer can accurately capture the fault information of the nearest bearing, whether it is EG or CG. This is consistent with practical experience and also validates the correctness of PCA.

Then, the K-Nearest Neighbor (KNN) algorithm ($k = 5$) is introduced for further analysis. Initially, a hold-out method is used with 70% of samples selected for training and 30% for testing. The confusion matrices of the CG and EG are presented in Fig. 15(a) and (b), respectively. The dominant diagonal elements (representing correct matches between predicted and actual labels) perform intensified blue in Fig. 15(b), demonstrating an improvement in classification accuracy from 81.94% for CG to 94.44% for EG. Subsequently, the recognition results of ten-fold cross-validation with different K values are compared in Fig. 15(c), with peak recognition rates of 97.9167% (EG) and 87.0833% (CG) achieved at $k = 5$. Finally, we also compare the recognition results of ten-fold cross-validation and five-fold cross-validation in Fig. 15(d). The results show that the accuracy of the EG exceeds 97%, whereas that of the CG remains below 88%, demonstrating the effectiveness of the encoding at the classification level.

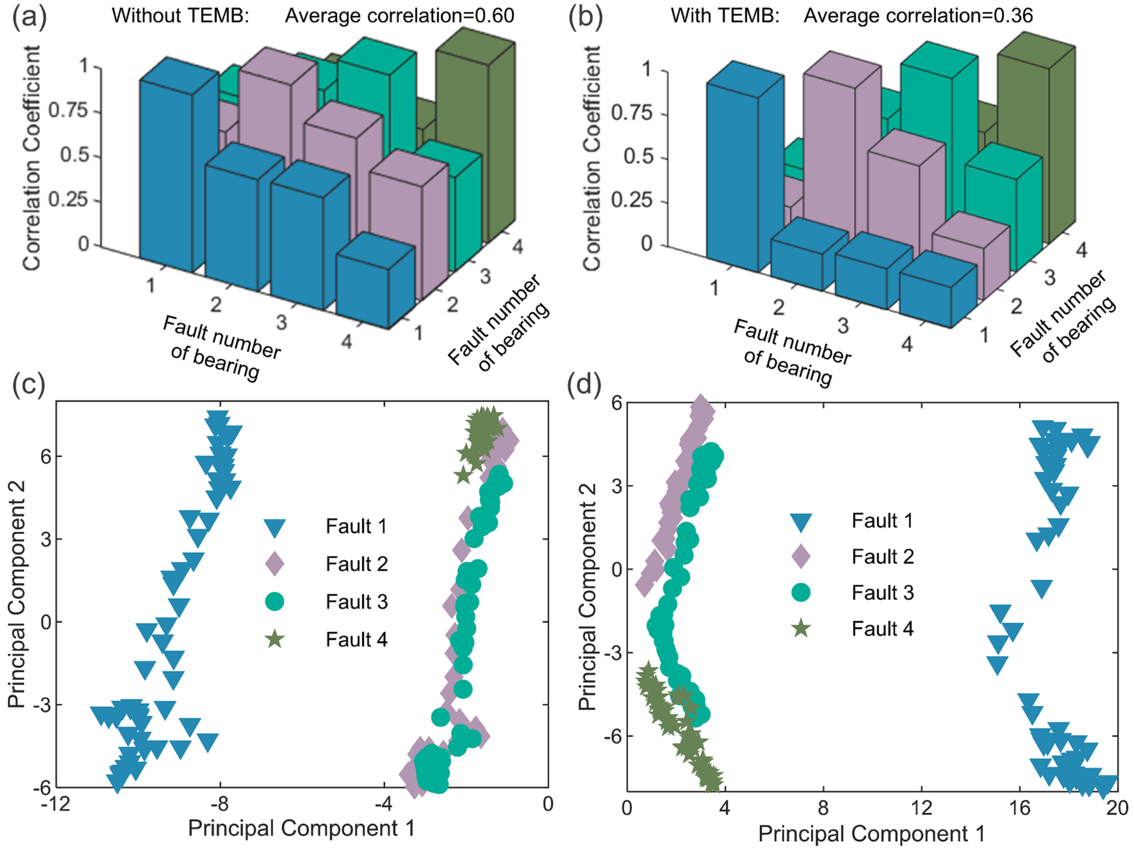

Fig. 14. Signal characteristics of the Control Group (CG) and Experimental Group (EG). (a) Correlation matrix for CG, with an average correlation of 0.60. (b) Correlation matrix for EG, showing a reduced average correlation of 0.36. (c) Principal Component Analysis (PCA) results for CG, where points corresponding to bearing 2, 3, and 4 faults are closely distributed. (d) PCA results for EG, revealing more distinct separation between different fault categories.

6. Discussion

In the proposed RLCM, the decreasing trend, rather than exact prediction of the resonant frequency, during the coupling process, is the key point to study. Consequently, the contact interactions across stiffness elements are neglected in FEM analysis, resulting in a frequency mismatch between FEM and experimental results. These interactions arise from the connection of the resonator, vary with the distance from the study point to the center of the resonator, and exhibit significant nonlinearity, bringing high complexity for analysis. With the decreasing trend validated in this study, precise dynamic models can be further developed in subsequent research.

Moreover, during the experiments, it was observed that the resonance peaks became less pronounced as coupling progressed. This effect could potentially be mitigated through a more suitable structural design, rather than being limited to the current plate-like configuration assembled using magnets.

In addition, as a conceptual model, TEMB is primarily designed to demonstrate its tunable encoding property. Due to the lack of systemically design, bandgap superposition as well as encoding frequency omission occur during development, weakening its influence on key system frequency characteristics. Information may become indistinguishable from unavoidable laboratory background noise, increasing the possibility of incorrect experimental identification. Therefore, careful parameter selection must be prioritized in engineering applications.

Finally, currently the layer switching of TEMB requires manual operation, which is inconvenient for application in complex systems. This might be processed in an automatic way when more mechanisms are introduced.

7. Conclusions

In this study, a resonant layer-coupling methodology (RLCM) is developed for in-situ tuning of resonator vibration properties. Unlike conventional approaches that realize bandgap tuning by directly or indirectly changing the stiffness or mass of the structure, the proposed method achieves tunability simply by stacking identical structural units to induce interlayer coupling. Through this stacking-induced interaction, RLCM enables simultaneous modulation of multiple resonators without altering their intrinsic mechanical

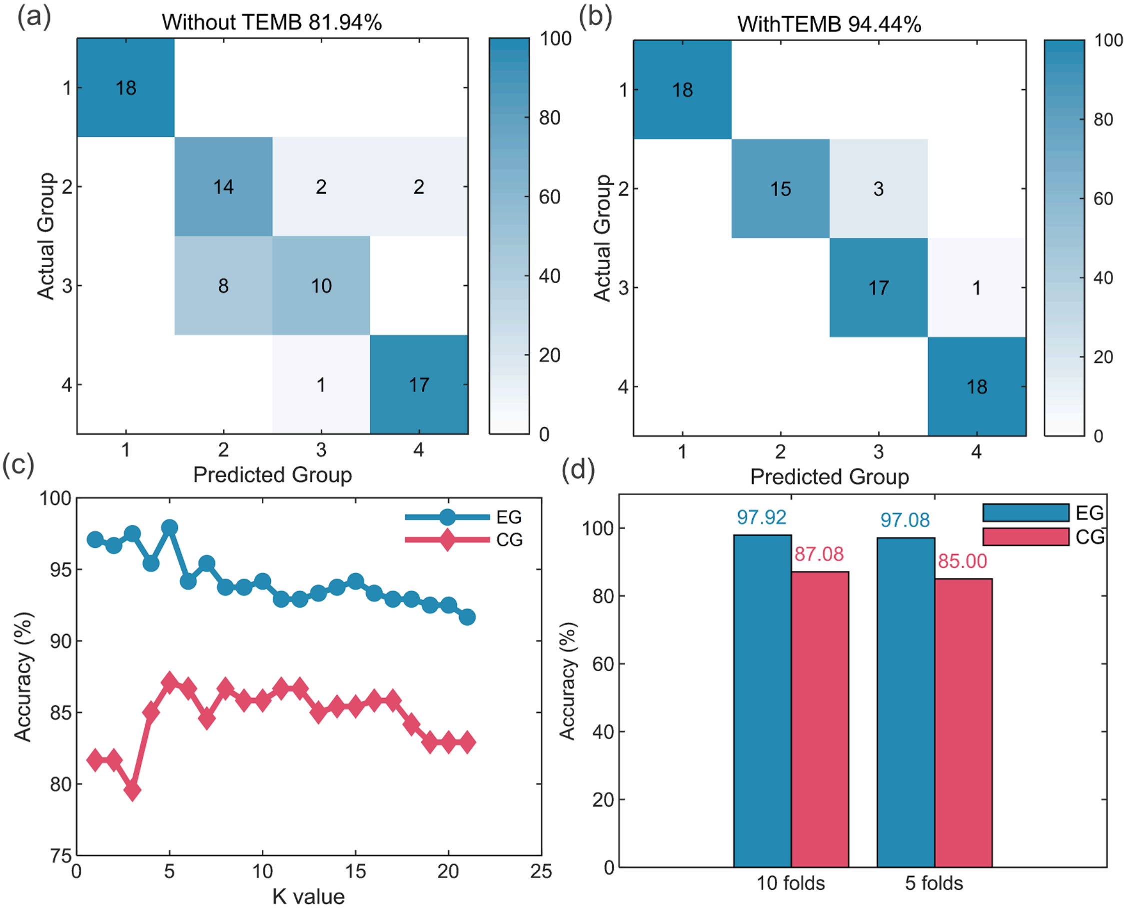

Fig. 15. Identification result for Control Group (CG) and Experimental Group (EG). (a) Confusion matrix for CG, where misclassification primarily occurs between bearing 2 and bearing 3, with a classification accuracy of 81.94%. (b) Confusion matrix for EG, showing an improved classification accuracy of 94.44%. (c) Recognition accuracies across different K values. (d) Recognition accuracies using ten-fold and five-fold cross-validations, achieving 97.92% and 97.08% accuracy for EG, and 87.08% and 85.00% for CG, respectively.

parameters, providing a physically consistent and easily implementable strategy that effectively simplifies bandgap control.

By enabling tunable resonant vibration characteristics through RLCM, the tunable encoding metamaterial box (TEMB) achieves superior integration compared to conventional schemes, thereby streamlining the design process and enhancing operational efficiency. Successfully applied in a rotor system with identical bearings, TEMB shows excellent potential for single-sensor fault localization, substantially improving the identification accuracy.

As a novel framework, RLCM integrates coupling dynamic idea with bandgap engineering to achieve elastic wave control through metamaterial. This groundbreaking paradigm is practical for addressing challenges in vibration suppression, acoustic mitigation, and waveform detection. With a detachable design that allows for flexible cross-platform deployment in other symmetrical mechanical systems, TEMB also shows promising application prospects in vibration source identification, fault diagnosis, and structural health monitoring. Future enhancements will focus on introducing precise dynamic models, smart tuning methods, and parameter optimization algorithms. By addressing current shortcomings, rapid effective tuning systems is hoped to be developed. Thereby, the proposed solutions will realize their value across a broad spectrum of engineering applications.

CRediT authorship contribution statement

Wenqu Li: Writing – review & editing, Writing – original draft, Validation, Methodology, Investigation, Conceptualization. **Yuhang Lin:** Investigation. **Tianqi Li:** Methodology. **Jingkai Huang:** Investigation. **Hao Huang:** Methodology. **Qingbo He:** Writing – review & editing, Supervision, Project administration, Funding acquisition, Conceptualization. **Zhike Peng:** Writing – review & editing, Supervision, Resources. **Li Cheng:** Writing – review & editing, Supervision.

Declaration of competing interest

The authors declare that they have no known competing financial interests or personal relationships that could have appeared to influence the work reported in this paper.

Acknowledgements

This work was supported in part by the National Natural Science Foundation of China under Grants No. 52275116, No. 12532001 and No. 12121002, the Program of Shanghai Academic/Technology Research Leader (22XD1421700), and the National High-Level Personnel of Special Support Program.

Supplementary materials

Supplementary material associated with this article can be found, in the online version, at doi:10.1016/j.jsv.2026.119899.

Appendix A

This appendix gives a comparison between the simulation and experimental results. The corresponding natural frequencies obtained from both approaches are summarized in Table A.1.

Table A.1
Comparison of simulation and experimental natural frequencies (Hz).

Resonator No.	One Layer		Two Layers		Three Layers		Four Layers	
	FEM	Experiment	FEM	Experiment	FEM	Experiment	FEM	Experiment
Resonator1	716	733	672	684	663	664	658	635
Resonator2	394	377	367	336	361	308	358	287
Resonator3	228	201	215	156	210	139	207	116
Resonator4	339	349	325	322	322	258	321	238
Resonator5	313	322	289	281	283	247	281	226
Resonator6	271	296	262	249	259	240	257	198

Data availability

Data will be made available on request.

References

[1] J.E. Marsden, T.S. Ratiu, Introduction to Mechanics and symmetry: a Basic Exposition of Classical Mechanical Systems, Springer Science & Business Media, 2013.

[2] S. Jiménez, M.O.T. Cole, P.S. Keogh, Vibration sensing in smart machine rotors using internal MEMS accelerometers, J. Sound. Vib. 377 (2016) 58–75.

[3] L. Rui, X. Ding, S. Wu, Q. Wu, Y. Shao, Signal processing collaborated with deep learning: an interpretable FIRNet for industrial intelligent diagnosis, Mech. Syst. Signal Process. 212 (2024) 111314.

[4] Q. Li, New sparse regularization approach for extracting transient impulses from fault vibration signal of rotating machinery, Mech. Syst. Signal Process. 209 (2024) 111101.

[5] L. Lin, M. He, W. Ma, Q. Wang, H. Zhai, C. Deng, Dynamic characteristic analysis of the multi-stage centrifugal pump rotor system with uncertain sliding bearing structural parameters, Machines 10 (2022) 473.

[6] M.V. van der Seijs, D. De Klerk, D.J. Rixen, General framework for transfer path analysis: history, theory and classification of techniques, Mech. Syst. Signal Process. 68 (2016) 217–244.

[7] B.K. Sinha, T.J. Plona, S. Kostek, S.K. Chang, Axisymmetric wave propagation in fluid-loaded cylindrical shells. I: theory, J. Acoust. Soc. Am. 92 (1992) 1132–1143.

[8] J. Lu, W. Cheng, D. He, Y. Zi, A novel underdetermined blind source separation method with noise and unknown source number, J. Sound. Vib. 457 (2019) 67–91.

[9] H. Tan, S. Xie, H. Zhou, W. Ma, C. Yang, J. Zhang, Sensible multiscale symbol dynamic entropy for fault diagnosis of bearing, Int. J. Mech. Sci. 256 (2023) 108509.

[10] K. Zhang, Y. Liu, L. Zhang, C. Ma, Y. Xu, Frequency slice graph spectrum model and its application in bearing fault feature extraction, Mech. Syst. Signal Process. 226 (2025) 112383.

[11] Z. Meng, Y. Wang, J. Liu, J. Li, F. Fan, Velocity-matching extraction demodulation transform for nonstationary signal analysis of rolling bearings, IEEe Trans. Instrum. Meas. (2024).

[12] X. Wang, H. Jiang, M. Mu, Y. Dong, A trackable multi-domain collaborative generative adversarial network for rotating machinery fault diagnosis, Mech. Syst. Signal Process. 224 (2025) 111950.

[13] T. Zhu, Y. Ren, H. Shi, Y. Ye, P. Feng, Z. Su, C. Yao, G. Ma, Wheel-rail force inversion via transfer learning-based residual LSTM neural network with temporal pattern attention mechanism, Mech. Syst. Signal Process. 224 (2025) 112135.

[14] T. Gao, J. Yang, Q. Tang, A multi-source domain information fusion network for rotating machinery fault diagnosis under variable operating conditions, Inf. Fusion 106 (2024) 102278.

[15] T.G. Chen, J.R. Jiao, D.J. Yu, Strongly coupled phononic crystals resonator with high energy density for acoustic enhancement and directional sensing, J. Sound. Vib. (2022) 529.

[16] M.-M. Shen, J.-H. Yang, D.-S. Yang, X.-D. Yang, Y.-J. Qian, Vibration control in bolted joints with locally resonant metamaterials, Int. J. Mech. Sci. 287 (2025) 109999.

[17] X. Zhang, J. Zhang, C. Xu, J. Rong, N. Hu, M. Deng, C. Zhang, Inverse-designed flexural wave metamaterial beams with thermally induced tunability, Int. J. Mech. Sci. 267 (2024) 109007.

[18] K. Chen, X. Dong, P. Gao, Q. Chen, Z. Peng, G. Meng, Physics-informed neural networks for topological metamaterial design and mechanical applications, Int. J. Mech. Sci. 301 (2025) 110489.

[19] T. Chen, D. Yu, A novel method for enhanced demodulation of bearing fault signals based on acoustic metamaterials, IEEE Trans. Ind. Inform. 18 (2022) 6857–6864.

[20] X.F. Zhu, B. Liang, W.W. Kan, Y.G. Peng, J.C. Cheng, Deep-subwavelength-scale directional sensing based on highly localized dipolar mie resonances, Phys. Rev. Appl. 5 (2016).

[21] T. Jiang, Q. He, Z.-K. Peng, Enhanced directional acoustic sensing with phononic crystal cavity resonance, Appl. Phys. Lett. (2018) 112.

[22] Y. Chen, H. Liu, M. Reilly, H. Bae, M. Yu, Enhanced acoustic sensing through wave compression and pressure amplification in anisotropic metamaterials, Nat. Commun. 5 (2014) 5247.

[23] T. Jiang, C. Li, Q. He, Z.-K. Peng, Randomized resonant metamaterials for single-sensor identification of elastic vibrations, Nat. Commun. 11 (2020) 2353.

[24] C. Li, T. Jiang, Q. He, Z. Peng, Smart metasurface shaft for vibration source identification with a single sensor, J. Sound. Vib. 493 (2021) 115836.

[25] T. Jiang, T. Zhou, X. Wang, T. Li, H. Jin, S. Zhang, Z.-K. Peng, Q. He, Spatial coding metastructure for single-sensor impact region recognition, Smart Mater. Struct. 33 (2024) 105041.

[26] X.X. Liao, T.X. Jiang, C. Li, X.L. Yu, Z.K. Peng, Q.B. He, Spatial-vibration-modulation-assisted blade damage localization for industrial quadrotor UAVs, Ieee Trans. Ind. Electron. 71 (2024) 2018–2027.

[27] X. Fang, J. Wen, B. Bonello, J. Yin, D. Yu, Ultra-low and ultra-broad-band nonlinear acoustic metamaterials, Nat. Commun. 8 (2017) 1288.

[28] Z. Zhai, Y. Wang, H. Jiang, Origami-inspired, on-demand deployable and collapsible mechanical metamaterials with tunable stiffness, Proc. Natl. Acad. Sci. 115 (2018) 2032–2037.

[29] S.M. Montgomery, S. Wu, X. Kuang, C.D. Armstrong, C. Zemelka, Q. Ze, R. Zhang, R. Zhao, H.J. Qi, Magneto-mechanical metamaterials with widely tunable mechanical properties and acoustic bandgaps, Adv. Funct. Mater. 31 (2021) 2005319.

[30] E. Dong, Z. Song, Y. Zhang, S. Ghaffari Mosanenzadeh, Q. He, X. Zhao, N.X. Fang, Bioinspired metagel with broadband tunable impedance matching, Sci. Adv. 6 (2020) eabb3641.

[31] A. Jamalimehr, M. Mirzajanzadeh, A. Akbarzadeh, D. Pasini, Rigidly flat-foldable class of lockable origami-inspired metamaterials with topological stiff states, Nat. Commun. 13 (2022) 1816.

[32] O.R. Bilal, A. Foehr, C. Daraio, Bistable metamaterial for switching and cascading elastic vibrations, Proc. Natl. Acad. Sci. 114 (2017) 4603–4606.

[33] C. Li, Z.K. Peng, Q.B. He, Stimuli-responsive metamaterials with information-driven elastodynamics programming, Matter 5 (2022) 988–1003.

[34] Z. Wei, Z. Hu, R. Zhu, Y. Chen, G. Hu, A transformable anisotropic 3d penta-mode metamaterial, Mater. Des. 234 (2023) 112306.

[35] Q. Lu, C.-c. Liu, Z. Qin, W. Ma, F.-m. Li, Vibration control and band gap tuning of finite periodic structure composed by active functionally graded metamaterial bars, Mech. Adv. Mater. Struct. 30 (2023) 856–869.

[36] L. Wang, Y. Liu, P. Du, T. Jiang, F. Ma, A. Tai, Chi acoustic metamaterial for low-dimensional joint compressive sensing and simultaneously azimuth-distance location, Mech. Syst. Signal. Process. 224 (2025) 112228.

[37] S.S. Rao, F.F. Yap, Mechanical Vibrations, Addison-Wesley, New York, 1995.